[illegible]
[illegible]
021 091

NASA-TM-112005

AIAA 95-1855
Application of a Navier-Stokes Solver to the Analysis of Multielement Airfoils and Wings Using Multizonal Grid Techniques

Kenneth M. Jones
NASA Langley Research Center
Hampton, VA

Robert T. Biedron
Analytical Services and Materials, Inc.
Hampton, VA

Mark Whitlock
Stanford University
Palo Alto, CA

13th Applied Aerodynamics Conference
June 19-22, 1995 / San Diego, California

APPLICATION OF A NAVIER-STOKES SOLVER TO THE ANALYSIS OF MULTIELEMENT AIRFOILS AND WINGS USING MULTIZONAL GRID TECHNIQUES

Kenneth M. Jones*
NASA Langley Research Center
Hampton, VA

Robert T. Biedron[†]
Analytical Services and Materials, Inc.
Hampton, VA

Mark Whitlock[‡]
Stanford University
Palo Alto, CA

Abstract

A computational study was performed to determine the predictive capability of a Reynolds averaged Navier-Stokes code (CFL3D) for two-dimensional and three-dimensional multielement high-lift systems. Three configurations were analyzed: a three-element airfoil, a wing with a full span flap and a wing with a partial span flap. In order to accurately model these complex geometries, two different multizonal structured grid techniques were employed. For the airfoil and full span wing configurations, a chimera or overset grid technique was used. The results of the airfoil analysis illustrated that although the absolute values of lift were somewhat in error, the code was able to predict reasonably well the variation with Reynolds number and flap position. The full span flap analysis demonstrated good agreement with experimental surface pressure data over the wing and flap. Multiblock patched grids were used to model the partial span flap wing. A modification to an existing patched-grid algorithm was required to analyze the configuration as modeled. Comparisons with experimental data were very good, indicating the applicability of the patched-grid technique to analyses of these complex geometries.

Introduction

Many technologies must be successfully integrated in the design of the next generation advanced subsonic transport. Among these are wing design, propulsion integration, design methodology and advanced high-lift systems. As subsonic transport designs get larger and issues such as airport tempo and noise abatement procedures become more important, the design of efficient high-lift systems becomes increasingly more important for improving the take-off and landing phase of the overall airplane mission. Additionally, improvements made in the design of the cruise wings also impacts the design of the high-lift system. Recently developed wing design technology allows designers to develop more efficient wings than those that exist on current subsonic transports. The performance benefits gained by this technology can be used to perform trade studies to improve the overall aircraft system. One way designers exploit these benefits is to reduce the size of the wing (which can help reduce the cost of the aircraft). This reduced wing area means the high-lift system must work even harder to achieve the necessary levels of lift to meet takeoff and landing requirements. More efficient high-lift systems would allow designers to take advantage of these new cruise wing designs. Therefore, the understanding of and ability to analyze these multielement high-lift systems is a problem that must be solved in order to allow the aircraft designer to develop a high-lift system which meets the required performance levels while still designing a wing which is easily integrated into the airplane configuration.

Researchers are currently investigating ways to use computational fluid dynamics (CFD) to improve the aerodynamic performance of these multielement high-lift systems. The difficulty in understanding and

---

[*] Aerospace Engineer, Aerodynamics Division. Senior Member AIAA.

[†] Aerospace Engineer, Aerodynamic and Acoustic Methods Division. Senior Member AIAA.

[‡] Student Member AIAA.

analyzing the flow over a three-dimensional high-lift system arises due to issues involving the complexity of the geometries and flow fields. Typical high-lift systems for current transport airplanes are geometrically complex, often consisting of a leading-edge slat and a multielement trailing edge flap system. Grid generation is made difficult due to the complexity introduced by the presence of the individual elements which must be modeled. Additionally, the relative positions of the elements in relation to the wing (gap distance, overhang distance, flap deflection) must be accurately described and modeled. The flowfield is also complex, due in part to the geometric complexity of the system. The flow from neighboring elements have pronounced impacts on the flow for other elements. If the flowfield is not accurately predicted over one element, the entire solution can be adversely affected. Another aspect of the difficult nature of the flowfield involves the fact that the geometries are operating in conditions which generate high levels of lift. This often occurs at moderately high angles of attack where viscous effects, such as flow transition and separation, may dominate the flowfield.

Researchers have attempted to approach the problem of high-lift system analysis many different ways. Some researchers have used inviscid three-dimensional analysis to examine the three-dimensional (3D) inviscid flow over typical transport aircraft high-lift systems (refs. 1,2). Some have used a combination of inviscid analysis with integral boundary-layer corrections (refs. 3,4). Many have approached the problem by performing Reynolds averaged Navier-Stokes analyses of two-dimensional (2D) airfoils (refs. 5–10) in order to understand the fundamental issues that are common between two and three-dimensional multielement flowfields. Two-dimensional analysis allows the researcher to study grid and flow solver issues on a slightly less complex level. The time required to create a 2D grid and perform multiple analyses is much less than that for a 3D grid. This not only permits researchers the opportunity to understand flow physics issues but also allows designers to optimize the airfoil shapes. The knowledge gained is then used for 3D design and analysis.

Two different types of grid schemes have been investigated for the Navier-Stokes flow solvers. One type is based on solving flows using structured grids to model the geometry and the other uses unstructured grids. Structured grid solvers are very robust, accurate and efficient and have been used to analyze many different types of geometries, both 2D and 3D. Unfortunately it is often time consuming and cumbersome to model complex high-lift systems using these techniques, particularly for cases involving geometry perturbations such as flap deflections and gap and overhang differences. The complexity issue becomes an even bigger challenge for 3D geometries. Unstructured grid methods hold a lot of promise due to the relative ease of grid generation and grid adaptation capabilities. Unstructured grids seem ideally suited for modeling very complex geometries. Although efficient, robust three-dimensional unstructured grid Navier-Stokes solvers are beginning to appear, all require substantially more memory than their structured grid counterparts. For large 3D problems, the memory requirements are generally prohibitive.

One way to reduce the difficulty of using structured grids to model complex geometries is to use multizonal grid techniques. A common multizonal approach is to use multiple-block grids with patching at grid boundaries or interfaces. This has proven to be a very robust and relatively efficient technique and has been employed by many researchers on many complex configurations. One of the common drawbacks is the amount of time required to generate the individual grid blocks and the requirement to insure that the grid boundaries match. A variation of the multizonal structured grid approach is known as the chimera[11] or overset grid approach. This approach is based on modeling geometries by creating as many individual grids around the geometry as necessary. Theses grids overlap each other and there is no attempt made to match the grids at the boundaries. A software package is then used to establish the necessary communication between the individual grids. Grid generation is made easier by the fact that each grid is generated individually having to enforce matching of the boundaries. Also, geometry perturbations are easily accounted for by simply moving the individual grid and rerunning the software that establishes the grid communications. This technique has been used for both 2D and 3D geometries.

This paper describes the application of a Reynolds averaged Navier-Stokes code in conjunction with two different multizonal-grid techniques for analysis of multielement flowfields. The Navier-Stokes code used for this study can be employed in the 2D or 3D mode. The first part of the paper describes the use of the chimera grid technique for the analysis of a 2D airfoil configuration. An assessment was made of the ability of the code to analyze details of the flowfield and to determine the sensitivity of the code to geometry and Reynolds number variations. The second part of the paper describes the use of the chimera technique for the analysis of a three-dimensional multielement high-lift wing with a full span flap. The third part of the paper demonstrates the use of a multiblock patched grid technique to analyze a high-lift wing with a partial span flap. A modification to an existing patched grid algorithm was developed in order to analyze the configuration as modeled.

Numerical Method

All computations were carried out using the Reynolds averaged Navier-Stokes code CFL3D.[12] CFL3D solves the unsteady, three-dimensional, compressible Navier-Stokes equations in their thin-layer approximation. The code employs an implicit, approximately-factored (AF) algorithm to advance the solution in time. The implicit spatial derivatives are upwind-biased first-order accurate, which results in a block tridiagonal inversion for each AF sweep. The explicit spatial derivatives use third-order upwind-biased differences for the inviscid terms, and second-order central differences for the viscous terms. Since spatial accuracy in the steady state is governed by the treatment of the explicit terms, the code is second-order accurate in space for steady flows. The upwind method used in this study was flux-difference splitting (FDS), although flux-vector splitting is also available in the code. For flows in which only the steady state is of interest (such as those considered here), savings in both memory and CPU time are obtained (without loss of accuracy) by using FDS in conjunction with a diagonal scheme, so that only scalar tridiagonal inversions are needed for each AF sweep. To accelerate convergence to a steady state the code can make use of grid sequencing, local time-stepping, and multigrid; the latter two techniques were utilized for all computations presented herein. For turbulent flows, CFL3D currently employs a number of different turbulence models, including Baldwin-Lomax,[13] Spalart-Allmaras[14] and the k-ω model of Menter.[15] All computations presented in this paper were carried out using the one equation Spalart-Allmaras model.

Grid generation was accomplished using a grid generator known as GRIDGEN.[18] The user generates algebraic grids on the faces of all the blocks (which are then smoothed with an elliptic solver). The GRIDGEN volume grid generator was then used to create the volume grids from these face grids. As with the face grids, the initial volume grid is generated using algebraic techniques but is then smoothed using elliptic solvers. For 2D calculations it was only necessary to generate planar grids.

CFL3D employs a number of zonal decomposition techniques to allow computations around arbitrary configurations with structured grids. Zonal interfaces may be point match (zones match exactly along a common interface), patched (zones share a common interface, but points do not need to match), or overset/chimera (zones overlap and do not share a common interface). All three types of zonal techniques have been utilized in the present analysis.

For patched and overset zones, data transfer between zones is accomplished by linear interpolation in the computational coordinate system. The required interpolation coefficients are obtained as a pre-processing step to the flow computation. In the case of overset grids, the interpolation stencils are generated by a software package known as MAGGIE.[16] MAGGIE is based on an early version of the program PEGSUS, modified by researchers at Old Dominion University to provide interpolation stencils at cell-center locations, as required for CFL3D, rather than at grid node points. More recently, the code has been modified to increase the speed and generality of the code, as well as to include two layers of fringe/outer boundary points for second-order accuracy. In the case of patched grids, the methods presented in reference 17 have been incorporated into a preprocessor known as RONNIE. For the current application to the partial span flap configuration, a minor modification to the RONNIE code was required, as discussed in the partial span flap section of the Results portion of the paper.

Typical resource requirements for three-dimensional computations using FDS and the diagonal scheme are approximately 35×10^{-6} seconds/grid point/iteration and 50 words/grid point using multigrid and a one-equation turbulence model. In two dimensions, approximately 15×10^{-6} seconds/grid point/iteration and 100 words/grid point are required; the higher memory requirement on a per grid point basis in two dimensions reflects a storage overhead that is generally negligible in three dimensions.

Results

Two Dimensional Airfoil

The geometry used for this study was a three element airfoil (slat, main element, and flap) that was designed by the Douglas Aircraft Company and tested in the Low Turbulence Pressure Tunnel (LTPT) located at the NASA Langley Research Center. The geometry was sent to several universities, aerospace corporations, and NASA sites as part of a NASA High-Lift CFD Challenge Workshop in 1993. The purpose of the CFD

Challenge was to define the state-of-the-art in 2D multielement airfoil prediction codes. This optimized airfoil and its extensive experimental aerodynamic database is currently being used throughout the aerospace industry as a means of calibrating CFD codes. The experimental database, reported on by Chin, et al.,[19] includes forces, velocity profiles, and total pressure profiles for two geometries at Reynolds numbers of 5 and 9 million.

Two airfoil configurations were studied in the CFD Challenge and they have been generally referred to as geometry A and geometry B. A list of the characteristics for the two airfoils is listed in the table below. The only difference between the two airfoils is the size of the gap between the main element and the flap. Geometry B has a small increase in flap gap when compared with geometry A. One of the issues involved in the CFD Challenge was to determine if the analysis codes could predict the difference in lift that is generated for this relatively small change in geometry. An additional part of the Challenge was to determine if the codes could predict the changes in lift that occur as a function of Reynolds number. For this paper geometry A was analyzed for Reynolds numbers based on chord of 5 and 9 million and geometry B at 9 million.

Geometry	A	B
Slat Deflection	-30^o	-30^o
Slat Gap	2.95%	2.95%
Slat Overhang	-2.5%	-2.5%
Flap Deflection	30^o	30^o
Flap Gap	1.27%	1.50%
Flap Overhang	0.25%	0.25%

A total of five grids were used to model the 3 element airfoil and are shown in fig. 1 for geometry A (for clarity only every other grid point is shown). Figure 1a and 1b show the two grids that were used to model the main element and main element flap cove region. A C-grid, shown in fig. 1a, was used around the main element and an H-grid (fig. 1b) was used to model the region from the main element flap cove to the downstream extent of the airfoil grids. This was done in an attempt to accurately model not only the cove region's backward facing step but also in order to accurately simulate the flow in the flap gap region. The slat and flap element grids are shown in fig. 1c. C-grids were used around the slat and flap and an H-grid was used to model the blunt trailing edge region behind the flap.

Wind Tunnel Walls - There is some concern that the wind tunnel wall corrections currently used in the LTPT become inaccurate at high lift coefficients, particularly near the maximum lift coefficient. Therefore, the best way to calibrate a code with this dataset is to use experimental data which has not been corrected for wall interference or tunnel blockage effects and model the wind tunnel walls. Cao[6] demonstrated the importance of modeling the wind tunnel walls in order to make an accurate comparison between computational results and experimental data. Results from Cao have shown that with the wind tunnel walls modeled, the location of the wake centerline is deflected upwards to conform to the shape of the tunnel walls. This effect would tend to keep the airfoil wake located in approximately the same location in the tunnel over a wide range of angle of attack. This allowed one grid to be used for all angles of attack, while still clustering the grid near the wake region. A plot of the tunnel grid with the 3 element airfoil is shown in fig. 2. The tunnel grid consists of 81 points in the streamwise direction and 65 points across the entrance and exit plane.

In addition to modeling the wind tunnel walls, appropriate boundary conditions must be set on all four boundaries of the grid. It was decided to model the tunnel floor and ceiling as inviscid surfaces since the boundary layer on the floor and ceiling are very thin and the airfoil is sufficiently far from any wall boundary layer that would exist. The downstream boundary condition was set by specifying the tunnel back pressure on the exit plane. This allowed for good control of the Mach number in the test section by simply varying the back pressure. The tunnel back pressure was determined using isentropic, one-dimensional flow equations (based on the desired test section Mach number). A characteristic inflow-outflow boundary condition was used for the tunnel inlet plane.

Grid Refinements - Rogers and Cao both discuss the issue of grid quality and its effect on the solution; not only the number of points but where they are located (i.e., the grid distribution). For the present analysis a similar study was conducted to investigate improvements in the chimera hole cutouts, grid clustering to better resolve the slat wake, and the effect of grid density on the flow solution. The grid study was computed for $\alpha = 16^o$, Reynolds number = 9×10^6, Mach number = 0.2 using the geometry A airfoil. Only one change was made to the grids at a time. This allowed the results to be compared to past solutions and determine what the effect of each change was. This approach allowed a better understanding of the effects of different grids and of the fluid physics around the airfoil.

Figure 3 is a plot of the original grid that was used to analyze the airfoil and the resulting velocity magnitude contours. Figure 3a is a close up of the main element grid in the region near the slat trailing edge and the main element wing under slat surface (wuss) region. The figure also shows the hole cutout that was made in the main element grid to account for the slat. The outline of the slat and slat grid is included to show the relative position and extent of the slat grid. The velocity magnitude contours calculated on the main element grid are plotted in fig. 3b. An examination of these contours show little impact of the slat flowfield on the main element flowfield immediately behind the slat, with a slightly more influence felt somewhat downstream of the slat. It is obvious that the momentum deficit resulting from the slat wake that was calculated from the slat grid is not being accurately communicated to the main element grid.

A number of modifications were made to the original grids to correct this problem and to improve the calculations over the entire airfoil geometry. First, the hole cutout in the main element grid due to the slat was extended further downstream. This had the effect of producing a larger region over which communication between grids occur. After further analysis of the resulting solution it was observed that the grid spacing in this region of the main element grid was not sufficient to accurately resolve the slat wake. To correct this problem, points were clustered in the main element grid near the predicted slat wake location. This was accomplished by using a solution-adaptive grid code and manually placing a source line near the location of the slat wake. This source line had the effect of clustering points on the main element grid to a location in the vicinity of where the source line was placed (i.e., in the region of the slat wake). The preceding modifications dealt with grid point placement. Another issue is overall grid density. A trade-off exists between computational costs and increasing grid density to improve the flow solution. The original grid contained nearly 70,000 grid points. For the purposes of this study, the grid density normal to the surface on the slat and main element grids was doubled, resulting in a grid which had a total grid size of approximately 106,000 grid points. The final grid and computed results are shown in fig. 4 (the grids shown in fig. 1 are also of this final grid). Figure 4a demonstrates the new cut out in the main element grid, the grid point clustering in the slat wake region and the doubling of points in the normal direction of the main element grid. There is a much more pronounced impact of the slat wake on the main element flow field using this new grid, as seen in fig. 4b.

A comparison between computational and experimental velocity profiles for two locations on the geometry is shown in fig. 5. Figure 5a shows comparisons for a location on the main element at the mid chord and fig. 5b is for the flap at the flap mid chord location. Figure 5a demonstrates the effects obtained by the changes that have been made to the grid on the main element flow field as compared with the original grid. The results obtained from the original grid show the slat wake very poorly resolved and an under prediction of the slat wake deficit (similar to what was seen in fig. 3b). The velocity profile obtained using the new grid does a much better job of resolving the slat wake. Unfortunately it tends to over predict the wake deficit. Similar results can be seen in fig. 5b. Again the new grid resolves all the wakes better than the old grid but over predicts not only the slat wake but the main element wake over the flap as well. Other authors have also seen this same tendency to over predict the wake deficits.

The pressure distributions around all three elements were also monitored with each change made to the grid. In all cases there were virtually no discernible changes to the distributions observed. The surface pressure comparison between theory and experiment for the final grid is shown in fig. 6 for $\alpha = 16^{\circ}$, Reynolds number = 9×10^{6}, Mach number = 0.2. There is good comparison between CFL3D and experiment for the flap surface pressures as well as for the surface pressures on the compression side of all three elements. The theory tends to slightly over predict the slat and main element suction peaks and the resulting adverse pressure gradient region. Even though the overall level of the region is over predicted, the character of the pressure distribution is well predicted, including the change in shape of the distribution at the end of the wuss region.

One parameter that was not varied in the grid refinement study was the number of grid points used in the circumferential direction. Rogers found that although circumferential spacing is important, normal direction spacing seemed to have a greater impact on the quality of the results.The number of grid points used in the circumferential direction for this study is on the order of that used by other researcher.[6,8] The over prediction of the suction peak seems to indicate that perhaps the circumferential spacing (distribution and/or number of points) needs to be studied, particularly in the leading edge region of the main element.

The total number of points used for the final 5 grids modeling the airfoil configuration was 106,425 points. The C-gird generated to model the main element (fig. 1a) used 321 points in the circumferential direction and 161 points in the normal directions. The H-grid for the flap cove region (fig. 1b) contained 97 points in the streamwise direction and 65 points in the normal direction. The C-grids for the slat and flap elements (fig. 1c) were dimensioned 225 × 145 and 225 × 65, respectively (circumferential × streamwise). Finally, the H-grid for the flap trailing edge region had 29 points in the normal direction and 41 points in the streamwise direction.

Angle of Attack - The airfoil (geometry A) was also analyzed for two different angles of attack for the same conditions of Reynolds number (9×10^6) and Mach number (0.2). The surface pressure distribution for $\alpha = 8^\circ$ is shown in fig. 7a and for $\alpha = 21^\circ$ in fig. 7b. The same trends that were seen at $\alpha = 16^\circ$ are seen for these two angles of attack. In all cases the lower surface pressures compare well with experimental data and the upper surface pressures are somewhat over predicted by theory, particularly for the slat and main element. Again the code does a very good job of picking up the character of the upper surface pressure distribution while being off by almost a constant increment in pressure coefficient.

Figure 8 contains comparisons of the section lift coefficients versus angle of attack for each of the three elements as well as the total section lift coefficient for this airfoil at a Reynolds number of 9 million. As expected based on the pressure distribution comparisons, the computed flap lift compares very well with experiment over this range of alpha. The computed slat lift is slightly over predicted and the main element lift is significantly higher than experiment. Additionally, there seems to be almost a constant increment in lift between theory and experiment over this angle of attack range with the difference in lift being slightly larger at the higher alpha. While the absolute level of the computed lift may not be in precise agreement with the data, the fact that the difference between computation and experiment remains relatively invariant with angle of attack suggests that trends can be reliably detected from the computations.

Effects Due To Reynolds Number and Flap Position - As stated earlier, two different Reynolds numbers and flap locations (involving a change in flap gap only) were tested. While absolute values of the results are most desirable, an almost equal desire is to be able to predict the trends caused by changes in Reynolds number and flap position. If the computational method can accurately predict these trends, designers of high-lift systems can use these methods to investigate flap position change sensitivity and to extrapolate wind tunnel results (which are often at less than flight Reynolds number) to flight Reynolds number conditions. The previous analysis was done for geometry A at a Reynolds number based on chord of 9 million. For the purpose of examining the above trends, the geometry A airfoil was analyzed at a Reynolds number of 5 million and the geometry B airfoil was analyzed at a Reynolds number of 9 million. The results of these analyses are seen in fig. 9. Figure 9a is a comparison between experimental data and CFL3D results for section lift coefficient versus angle of attack for geometry A at a Reynolds number of 5 million while 9b is for the geometry B airfoil at a Reynolds number of 9 million. Both figures demonstrate the same trends that were seen for the geometry A airfoil at a Reynolds number of 9 million. The flap lift comparisons are very good and the slat comparisons are only slightly off. Just as with the previous results, the calculated main element lift values are higher than experiment and also as before, the difference appears to be an almost constant increment with slightly larger differences seen at $\alpha = 21^\circ$.

The experimental and theoretical trends of lift versus angle of attack are seen in fig. 10. In fig. 10 there are two trends plotted. The trend labeled A9-A5 is the difference between the lift coefficient for geometry A at a Reynolds number of 5 million and the lift coefficient for geometry A at a Reynolds number of 9 million (Reynolds number trend). Similarly the trend labeled A9-B9 is the difference between the lift coefficient for geometry B and the lift for geometry A, both at a Reynolds number of 9 million (flap rigging trend). The code correctly predicts that as Reynolds number is increased (A9-A5) there is an increased level of lift generated on the airfoil. The theory does however under predict the amount of this lift increment. The code tends to do a better job picking up the effect of the flap rigging change (A9-B9) with some discrepancy at $\alpha = 21^\circ$.

Three Dimensional Wing

One of the primary objectives of this research is to evaluate and develop techniques which would enable a researcher to analyze a complex three-dimensional multielement high-lift system on a subsonic transport configuration. The analysis of the airfoils, discussed in the previous section, was done in part to gain experience and confidence with issues that occur on two and three-dimensional problems. In this section, three-dimensional high-lift systems that were analyzed using structured grid techniques will be discussed. A wing based on a NACA 0012 airfoil section with a single element Fowler flap was analyzed. Both full span and partial span flap configurations were investigated. The experimental data of Weston[20] was used for comparison of the partial span flap configuration. For the full span flap, the experimental data obtained by Applin[21] was used for comparison with computational results.

Full Span Flap Configuration - The configuration chosen for the initial three-dimensional analysis was the full span Fowler flap wing. The model span was 9.68 feet and the chord for the stowed configuration was 3.28 feet. The flap had a 1 percent (based on stowed chord) overhang, a 2.5 percent (again based on stowed chord) gap between the flap and main element and was deflected nominally 30 degrees. The wing was tested in a semispan mode in the 14 x 22 Foot Subsonic Tunnel at the NASA Langley Research Center as shown in fig. 11a. Since the configuration was mounted on the floor of the tunnel, during the test a floor boundary layer removal system was used to reduce the effect of the floor boundary layer on the model flowfield. A description of the tunnel and boundary layer removal system can be found in reference 22. The model was equipped with 600 pressure taps at 10 span locations along the wing (fig. 11b). Additionally, a wake rake consisting of seven parallel 5-hole probes was used to measure wake velocity and pressure in the flowfield downstream of the models tested.

For this configuration a chimera grid technique was chosen. As with the airfoil analysis, the first step was to generate a grid around the different elements. In this case volume grids were created for the main element and Fowler flap. The main element grid consisted of 321 points around the airfoil, 49 points along the span and 81 points in the normal direction from the surface, with the outer boundary located 20 chords from the surface of the airfoil. The flap had 121, 49 and 33 points around the airfoil, out the span and in the normal direction, respectively. The combined grids used a total of 1.47 million grid points. The grid spacing was clustered in the normal direction to insure a maximum y^+ value of 1. The chimera preprocessing code MAGGIE was again used to create the appropriate "holes" and interpolation stencils. Figure 12 shows the final grid including the main element and flap surface grids, a streamwise plane of the main element grid (with a hole cut out for the flap) shown on the plane of symmetry and a grid plane from the flap grid (with a hole cut out for the main element) shown about 2/3 of the way out toward the tip of the flap. These grids were then analyzed using CFL3D for a Reynolds number of 3.3×10^6, at a Mach number of 0.15, and angles of attack of 4 and 8 degrees. It should be pointed out that for this study the wind tunnel walls were not modeled, and the floor of the tunnel was treated as an inviscid plane of symmetry.

A comparison between theory and experiment for the surface pressure distributions is shown in fig. 13. Figure 13a contains comparisons at five semispan locations ($\eta = y/b$, where b=116.01 inches is the model semispan) on the wing for $\alpha = 4^o$ and a plot of the airfoil section of the main element and flap. The flap and flap pressures have been unrotated and translated downstream for clarity. The comparisons are very good for all the semispan locations with some degradation of the agreement near the wing tip. The main element and flap leading edge suction peaks are well captured by the code as are the overall levels of surface pressure. The only significant differences occur near the trailing edge of the main element, the upper surface pressure distribution on the flap and the flap pressures near the tip of the wing. There is an expansion near the trailing edge of the main element that is not accounted for by the code. This expansion is most likely due to the influence of the flap on the main element. It is possible that if the hole cut out on the grids or the grid density in the trailing edge/flap-gap region were changed, the expansion might be better predicted. The code does a good job picking up the separation that occurs on the aft portion of the flap but does tend to slightly under predict the level of pressure on the upper surface of the flap. The rapid expansions of pressure out near the tip of the wing indicate the presence of wing tip and flap tip vortices. The code does a good job of picking up the wing tip expansions on the upper surface of the main element and does pick up the character of the pressure distribution for the flap surface pressure but over predicts the peak and recovery of the pressure on the flap tip. These same comparisons between theory and experiment can be seen for the $\alpha = 8^o$ case shown in fig. 13b.

To get a better idea of the surface flowfield characteristics for this wing at these two angles of attack, surface streamlines were plotted on a grid plane just off the surface of the configuration (fig. 14). The surface streamlines indicate that the flow is basically streamwise on most of the main element for $\alpha = 4^o$ (fig. 14a). The streamlines also show significant turning of the flow around the wing tip indicative of a wing tip vortex. The streamlines for the flap show a significant separated flow region that occurs near the 50% flap chord location and continues over the entire span of the flap. This separated region diminishes slightly near the wing tip. Near the tip of the flap a rapid turning of the flow is evident as is a separation line, indicating the presence of a flap tip vortex. These same trends occur at $\alpha = 8^o$ with a slightly larger region of separated flow on the flap (fig. 14b). These trends correlate well with the surface pressure data of fig. 13.

As mentioned previously, wake pressure data were taken during the test. Qualitative comparisons made between the theoretical results and off body pressure data should give some additional insight into the ability of the code to analyze the wakes and tip vortices being shed from the main element and flap. Figure 15 shows a comparison of computed and measured total pressure coefficient contours for two locations behind the configuration at $\alpha = 4^o$. The origin of the coordinate system used for the wake rake system is located at the flap trailing edge. Therefore $x/c = 0.1$ is 0.1 chords behind the flap trailing edge and $z/c = 0.0$ is located at the same height as the flap trailing edge. The experimental data for $x/c = 0.1$ indicates the presence of two vortices (as expected from the previous discussions). The corresponding computational results show a slightly elongated pressure contour but do not show the presence of two distinct vortices. After further examination of these contours overlaid on top of the grids in this region it was apparent that the grid density off the surface of the flap was not sufficient to resolve these two distinct vortices. The presence of the two vortices was seen close to the location where they were formed but they quickly merge into one. Great care must be taken during the grid generation process to place a sufficient number of points in this region to allow resolution of these distinct vortices. Examples such as this one (and the airfoil wakes discussed above) indicate the importance of developing automatic grid adaptation techniques that can cluster points in areas of high flow gradients. At $x/c = 0.5$ (fig. 15b) the experimental data seem to indicate the two vortices are beginning to merge together. The computational results again show only the presence of a single vortex.

Partial Span Flap Configuration - The partial span flap wing tested by Weston was also analyzed using CFL3D. The configuration is similar to the full span flap wing except that the outboard 58% of the wing has the flap in the stowed position. All other aspects of the configuration are the same, including the flap deflection, overhang, gap and pressure tap locations. A photograph of the wing mounted in the 14 x 22 Foot Subsonic Tunnel is shown in fig. 16. As with the full span flap configuration, the wind tunnel test was run with the tunnel floor boundary layer removal system on. Surface pressure and wake pressure data were again taken during the test.

A partial view of the grids used to analyze the configuration are shown in fig. 17. There were a total of five C-grids used to model this geometry; three for the inboard multielement region, one for the outboard stowed flap region and one for the wing tip. The three grid blocks used in the flap region consisted of an inner grid around the main element (321 points circumferentially, 33 normal, 33 spanwise), an inner grid around the flap ($193 \times 49 \times 33$) and an outer grid ($337 \times 49 \times 33$) that enclosed the two inner grids. This arrangement was necessary in order to insure good grid resolution of the individual elements. Point to point matching along the grid boundaries was used for the three blocks that model this inboard region. A fourth grid was used to represent the wing in the region from the spanwise discontinuity of the wing to the beginning of the wing tip and consisted of $337 \times 81 \times 33$ points (circumferential, normal and spanwise). A fifth and final block was used to model the wing tip and the flowfield outboard of the wing tip. Again this block had 337 points circumferentially and 81 points in the normal direction. There were a total of 25 spanwise points with 9 points on the wing tip. Figure 17 shows the plane of symmetry grid and the surface grids for the inboard multielement region and the outboard portion of the configuration. The complete grid consisted of 2.79 million grid points.

For the partial span flap configuration, the flap and outboard undeflected wing section meet along an essentially gapless interface in the spanwise direction. Two different approaches may be taken to model the spanwise geometry discontinuity along this streamwise flap/undeflected wing section juncture (referred to in the rest of this paper as the "juncture region"). The first is to widen the gap enough to allow one or more grid zones to be placed between the flap and the outboard wing. The second approach, adopted here, is to reduce the gap to zero so that the flap zone and outboard wing zone are patched along a common interface in the juncture region. This makes the grid generation task much simpler, but introduces a slight complication for the patched-grid preprocessor.

Figure 18 illustrates the situation that arises when attempting to transfer data from the grid surrounding the outboard undeflected wing (donor mesh) to the flap grid. Although not_shown, a similar situation arises when transferring data from the flap grid to the outboard wing grid. In general, for each cell center in the receiving mesh (e.g., the flap grid), a search is made in the donor mesh to find the appropriate cell from which the required data may be interpolated. However, in the situation illustrated in fig. 18, a number of cells in the flap grid lie outside the domain of the donor mesh (i.e., inside the outboard wing), and hence cannot be found by the search algorithm. Ordinarily, this would cause the search algorithm to fail; however, the algorithm was modified to simply mark such cells as being "found" in a non-existing block (e.g., block 0), and to be given interpolation coefficients of zero. These "orphan" points are then output along with the points having valid interpolation coefficients (i.e., those that were actually found in the donor mesh) to a zonal interpolation file that is used by the flow solver. CFL3D is coded in such a way that physical boundary conditions (e.g., no slip, inflow/outflow, etc.) are set first, then the zonal interpolation files are read in and used to set the boundary conditions, via interpolation, for all points contained in the zonal interpolation files. Thus the technique used for setting the boundary conditions on the flap edge is to first set the entire flap face to no slip. When the zonal interpolation file is read in, the points that get interpolated from bonefide blocks (e.g., block numbers > 0) will overwrite the no-slip values with data interpolated from the donor mesh. Because the orphan points are identified with a non-existing donor block, they, in fact, never get changed from their no-slip values. Thus the final boundary conditions on the edge of the flap grid are as shown in fig. 18: no slip for those points that lie on the edge of the juncture region but inside the curve defining the outboard wing surface, and interpolation from the outboard wing grid for those points lying outside the curve defining the surface.

While the procedure described above formally enforces the no-slip condition in the correct location, any boundary layer on the edge of the flap will only be accurately captured if the spanwise spacing in this region is sufficiently fine. For the grids considered in this study, the spanwise spacing near the juncture region was very coarse, and so the flap and outboard wing edges are effectively inviscid.

A comparison between theory and experiment for the surface pressure distributions is shown in fig. 19. Figure 19a contains surface pressure distribution comparisons at four semispan locations on the wing for $\alpha = 4^o$, two of which are located inboard of the juncture region and two outboard. The juncture region is at a semispan location (η) of 0.58. Plots of the airfoil sections for the flap region and stowed flap region of the wing are shown for illustrative purposes. The flap is translated downstream for clarity. The code does a very good job of predicting the pressure distributions at all four locations shown. These computations even pick up the slight expansion near the trailing edge that is caused by the presence of the flap flowfield (η = .185 and η = .472). There is some slight under prediction of the pressure peaks on the leading edge of the flap but this is most likely a result of poor flap leading edge definition. The computations also pick up the region of separated flow that exists near the trailing edge of the flap. Similar comparisons can be seen for the $\alpha = 12^o$ case. It should be noted that the pressure distribution comparisons are very good even near the juncture region (comparisons at η = .472 and η = .601).

The surface streamline patterns (fig. 20) demonstrate the three dimensional nature of the surface flowfield for $\alpha = 4^o$ and $\alpha = 12^o$. For the 4 degree case, fig. 20a, the separated region of flow on the flap is quite evident. Unlike the full span flap case, this separation region is slightly further aft on the flap and involves more spanwise variation. The separation region diminishes dramatically as the juncture region is approached. There is also some turning of the flowfield on the outboard undeflected wing near this juncture region. As in the full span flap case, there is significant turning of the flow around the tip of the wing indicative of a wing tip vortex. These same trends become more pronounced at $\alpha = 12^o$. The separation region is slightly smaller on the flap and there appears to be a small region of separated flow near the trailing edge on the outboard portion of the wing near this juncture region. In addition, there is more turning of the flow near the wing tip than there was at 4 degrees angle of attack.

Wake rake measurements were also taken during the test of this partial span flap configuration and a comparison between computationally and experimentally obtained total pressure coefficient contours is shown for two locations downstream of the wing for $\alpha = 4^o$. The origin of the wake rake system is again centered at the flap trailing edge location. The comparisons are very good for an x/c location of 0.1 (fig. 21a). The code has properly captured both the horizontal and vertical position of wing tip vortex and the vortex that originates from the flap. The code also predicts the proper location of the wakes from the flap and outboard wing trailing edges. These same good correlations are seen even at an x/c location of 0.5 (fig. 21b) with a possible small discrepancy between the size of the vortices computed with the code compared with the experimentally measured data. The grid density is beginning to decrease in this region resulting in slightly less resolution of the vortices. Again, in light of the approximations that were employed in the implementation of this new technique, these results are very encouraging as to the applicability of the preprocessor modifications for analyzing these partial-span configurations.

Summary

A computational study was performed to determine the predictive capability of a Reynolds averaged Navier-Stokes code (CFL3D) for two-dimensional and three-dimensional multielement high-lift systems. Three configurations were analyzed: a three-element airfoil, a wing with a full span flap and a wing with a partial span flap. In order to accurately model these complex geometries, two different multizonal structured grid techniques were employed. For the airfoil and full span wing configurations, a chimera or overset grid technique was used. Multiblock patched grids were used to model the partial span flap. A modification to an existing patched-grid algorithm was required to analyze the configuration as modeled.

The three element airfoil computations were performed using a total of six grids; five representing the airfoil geometry and one grid to simulate the wind tunnel. A grid refinement study was conducted to improve the results, particularly the communication between the slat flowfield and the main element flowfield. It was found that improving the shape of the chimera hole cut out and improving the grid density and distribution had a dramatic effect on the downstream flowfield velocity profiles. Although the correct characteristics of the flowfield were obtained by the analysis, the pressure distributions and integrated lift coefficient values were somewhat over predicted in this study. A comparison of the lift versus angle of attack for each individual element showed that the greatest discrepancy between theory and experiment occurred for the main element. One possible explanation might be the grid distribution in the leading edge region of the main element and may require different clustering of the grid in the circumferential direction. Even though the absolute values of lift were somewhat in error, the code was able to predict reasonably well the variations with Reynolds number and flap position.

The application of the chimera technique to the analysis of a simple wing with a full span Fowler flap was analyzed for a Mach number of 0.15 and angles of attack of 4 and 8 degrees. The experimental and computational surface pressure distributions agree very well over the entire wing. The code was able to accurately compute the leading edge suction peaks for both elements and did a good job predicting the effect of the tip vortices on the two elements. Computationally obtained surface streamlines demonstrated the presence of a separated flow region on the aft portion of the flap which agreed well with trends indicated by the surface pressure distributions. Qualitative comparisons were made between experimentally obtained wake pressure measurements and those predicted by the code. Although the code predicted the general location of the vortices that are shed from the wing tip and flap tip, at the location where the experimental data are taken, the grids were not sufficiently dense to resolve the two distinct vortices.

A partial span flap wing configuration was analyzed using a multiblock grid technique. The geometry was modeled using a total of five C-grids; three for the inboard multielement region of the wing, one for the outboard undeflected flap region of the wing and one for the wing tip. Point to point matching was used for the three blocks used to model the inboard region. Rather than try to enforce point to point matching across the spanwise discontinuity in the geometry between the inboard and outboard part of the wing, patching was used between the different grid blocks at that interface. A modification was made to the patched-grid preprocessor to account for this spanwise variation in the grids without requiring the user to explicitly model the side of the flap and allowing a zero gap between the multielement portion of the wing and the stowed flap portion of the wing. This greatly simplified the grid generation task. The results obtained from CFL3D using these modifications are very good. Surface pressure distribution comparisons between theory and experiment demonstrated very good correlation between the two, even near the region of the geometry discontinuity. The code also predicted very reasonable surface streamline patterns and predicted areas of separated flow on the flap and on the main wing near the partial span flap juncture. Wing tip and flap tip vortices downstream of the configuration are also well predicted by the code. These results are very encouraging, indicating the applicability of the patched-grid technique to analyses of these complex geometries.

Acknowledgments

The authors would like to thank the many researchers who contributed ideas and assistance to the creation of this paper, particularly members of the Subsonic Aerodynamics Branch at the NASA Langley Research Center. The authors would also like to thank Mr. William Jones of the Computer Sciences Corporation and Dr. Balasubramanian of Spectrex, Inc. for their help in generating the partial span flap grid.

References

[1]Dodbele, S., "Three Dimensional Aerodynamic Analysis of a High-Lift Transport Configuration," AIAA Paper 93-3536, Aug. 1993.

[2]Valarezo, W. and Chin, V., "Maximum Lift Prediction for Multielement Wings," AIAA Paper 92-0401, Jan. 1992.

[3]Drela, M., "A User's Guide to MSES V2.3," Feb. 1993.

[4]Hardin, J., Potter, R., van Dam, C., and Yip, L., "Two-Dimensional Computational Analysis of a Transport High-Lift System and Comparison with Flight-Test Results," AIAA Paper 93-3533, Aug. 1993.

[5]Mavriplis, D., "Turbulent Flow Calculations Using Unstructured and Adaptive Meshes," NASA CR-182102, 1990.

[6]Cao, H., Kusunose, K., Spalart, P., Ishimitsu, K., Rogers. S., and McGhee, R., "Study of Wind Tunnel Wall Interference for Multi-Element Airfoils Using a Navier-Stokes Code," AIAA Paper 94-1993, June 1994.

[7]Rogers, S., Menter, F., Durbin, P., and Mansour, N., "A Comparison of Turbulence Models in Computing Multi-Element Airfoil Flows," AIAA Paper 94-0291, Jan. 1994.

[8]Rogers, S. E., "Progress in High-Lift Aerodynamic Calculations," *Journal of Aircraft*, Vol. 31, No. 6, P1244–1251, Nov.–Dec. 1994.

[9]Dominik, C., "Application of the Incompressible Navier-Stokes Equations to High-Lift Flows," AIAA Paper 94-1872, June 1994.

[10]Anderson, K. W., "Navier-Stokes Computations and Experimental Comparisons for Multielement Airfoil Configurations," AIAA Paper 93-0645, Jan. 1993.

[11]Benek, J., Buning, P., and Steger, J., "A 3-D Chimera Grid Embedding Technique," AIAA Paper 85-1523-CP, July 1985.

[12]Thomas, J., Krist, S., and Anderson, W., "Navier-Stokes Computations of Vortical Flows Over High Aspect-Ratio Wings," *AIAA*, Vol. 28, No. 2, pp. 205–212, Feb. 1990.

[13]Baldwin, B. and Lomax, H., "Thin Layer Approximation and Algebraic Model for Separated Turbulent Flow," AIAA Paper 78-257, 1978.

[14]Spalart, P. and Allmaras, S., "A One-Equation Turbulence Model for Aerodynamic Flows," AIAA Paper 92-0439, 1992.

[15]Menter, F. and Rumsey, C., "Assessment of Two-Equation Turbulence Models for Transonic Flows," AIAA Paper 94-2343, 1994.

[16]Lessard, V., "Domain Decomposition for Multigrid, Finite Volume Flow Solvers," Master's Thesis, Old Dominion University, Dec. 1989.

[17]Biedron, R. and Thomas, J., "A Generalized Patched-Grid Algorithm With Application To The F-18 Forebody With Actuated Control Strake," *Computing Systems in Engineering*, Vol. 1, Nos. 2–4, pp. 563–576, 1990.

[18]Steinbrenner, J. and Chawner, J., "The GRIDGEN Version 8 Multiple Block Grid Generation Software," MDA Engineering Report 92-01, May 1993.

[19]Chin, V., Peters, D., Spaid, F., and McGhee, R., "Flowfield Measurements about a Multi-Element Airfoil at High Reynolds Numbers," AIAA Paper 93-3137, July 1993.

[20]Weston, R., "Refinement of a Method for Determining the Induced and Profile Drag of a Finite Wing From Detailed Wake Measurements," Doctoral Dissertation, University of Florida, 1981.

[21]Applin, Z., "Pressure Distributions From Subsonic Tests of a NACA 0012 Semispan Wing Model," NASA TM-110148, February 1995.

[22]Gentry, G., Jr., Quinto, P., Gatlin, G., and Applin, Z., "The Langley 14- by 22-Foot Subsonic Tunnel: Description, Flow Characteristics, and Guide for Users," NASA TP-3008, July 1993.

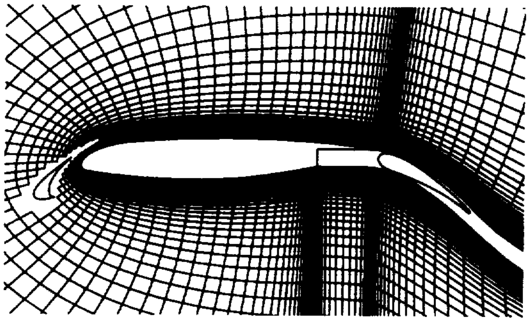

Fig. 1a. 3 element airfoil main element grid.

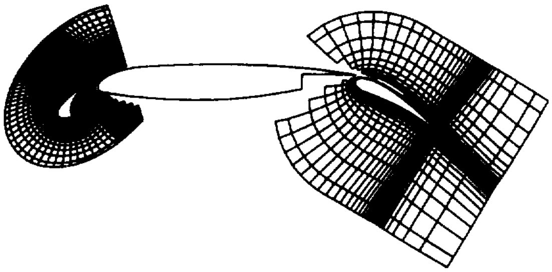

Fig 1c. 3 element airfoil slat, flap and flap trailing edge grids.

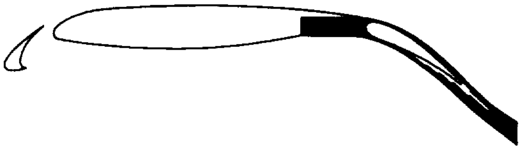

Fig 1b. 3 element airfoil cove grid.

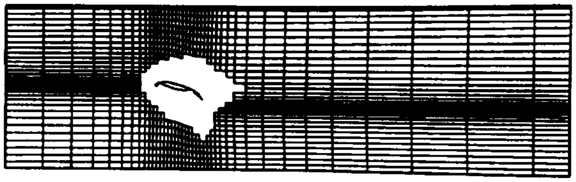

Fig. 2 Tunnel grid.

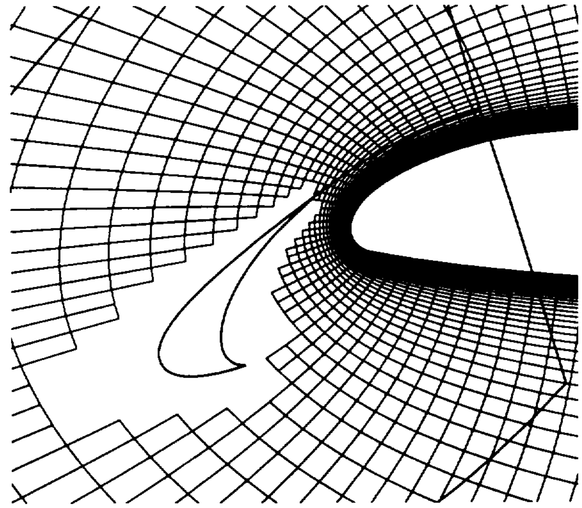

Fig. 3a. Original main element grid.

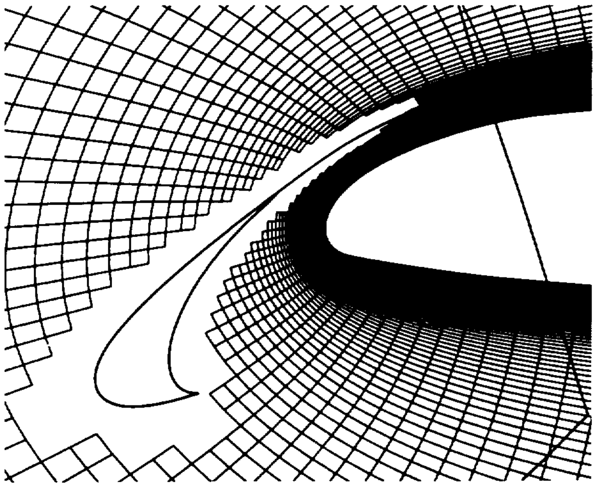

Fig. 4a. Final main element grid.

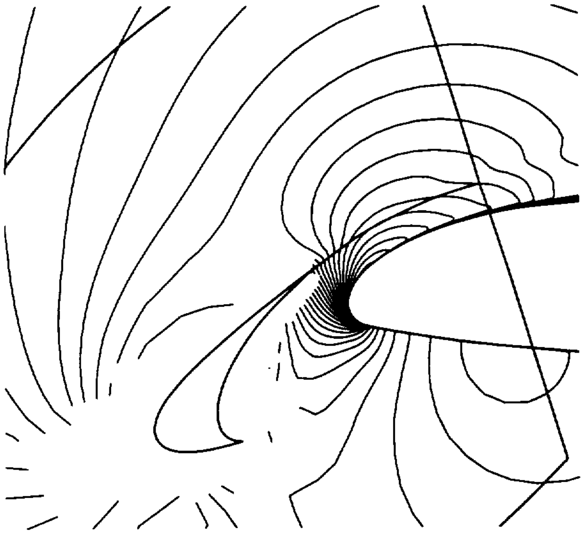

Fig. 3b. Velocity magnitude contours for the original grid, $\alpha = 16$, $M = .2$, $R_e = 9 \times 10^6$.

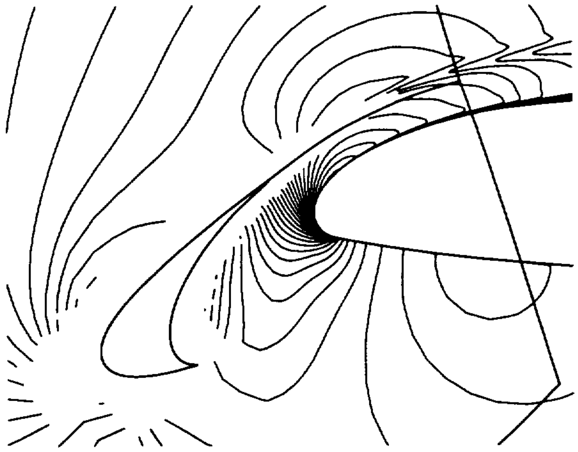

Fig. 4b. Velocity magnitude contours for the final grid, $\alpha = 16$, $M = .2$, $R_e = 9 \times 10^6$.

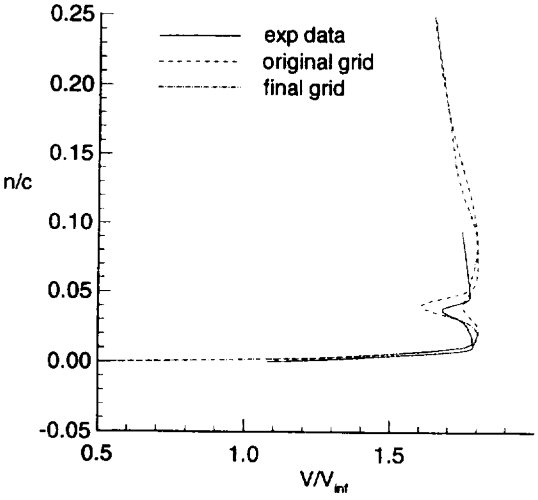

Fig. 5a. Velocity profiles over the main element, $\alpha = 16$, $M = .2$, $R_e = 9 \times 10^6$.

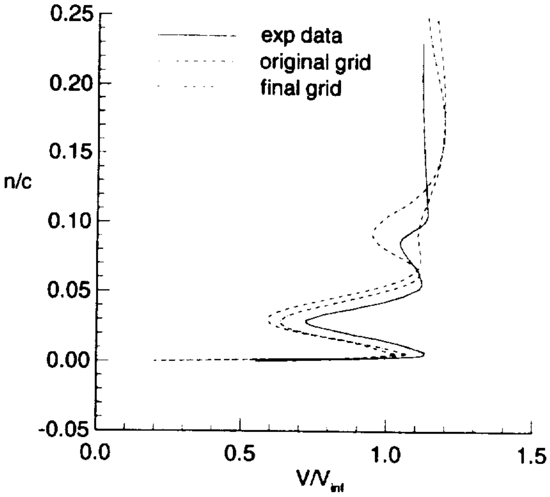

Fig. 5b. Velocity profiles over the flap element, $\alpha = 16$, $M = .2$, $R_e = 9 \times 10^6$.

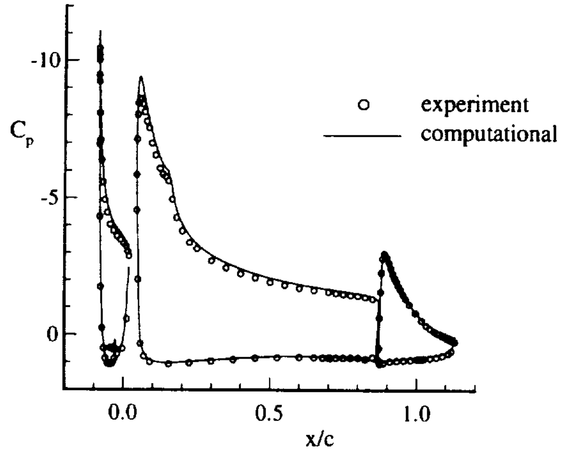

Fig. 6. Pressure distribution, $\alpha = 16$, $M = .2$, $R_e = 9 \times 10^6$

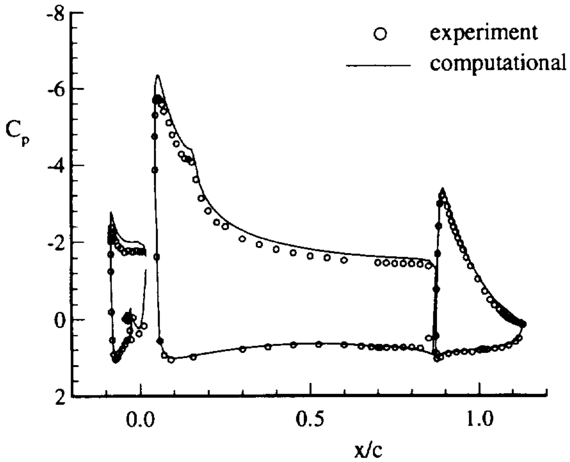

Fig. 7a. Pressure distribution, α = 8, M = .2, $R_e = 9 \times 10^6$.

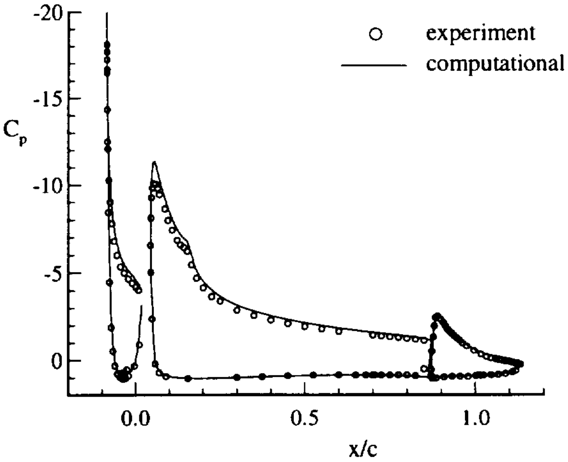

Fig. 7b. Pressure distribution, α = 21, M = .2, $R_e = 9 \times 10^6$.

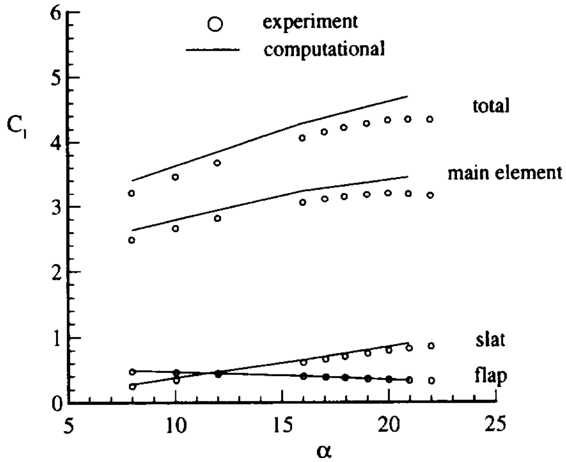

Fig. 8. Lift curve, geometry A, M = .2, $R_e = 9 \times 10^6$.

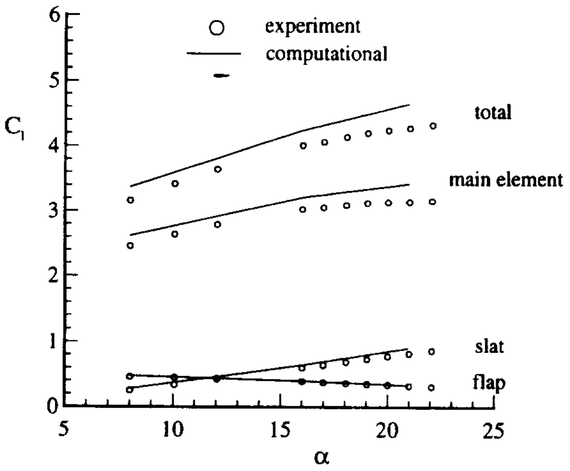

Fig. 9a. Lift curve, geometry A, M = .2, $R_e = 5\times 10^6$.

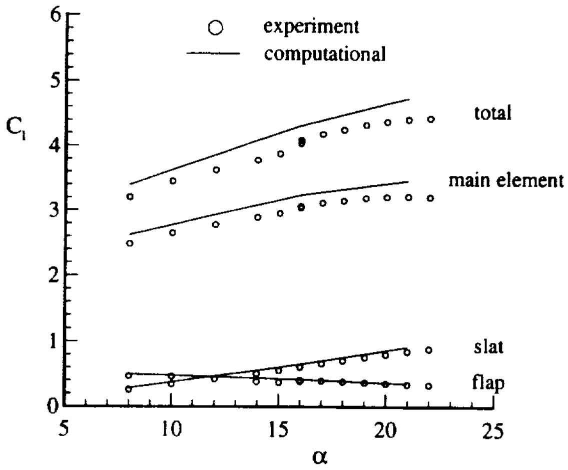

Fig. 9b. Lift curve, geometry B, M = .2, $R_e = 9 \times 10^6$.

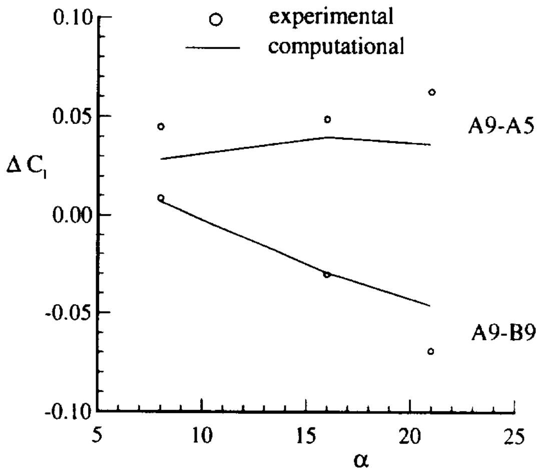

Fig. 10. ΔC_l vs. α for different Reynolds number and geometry.

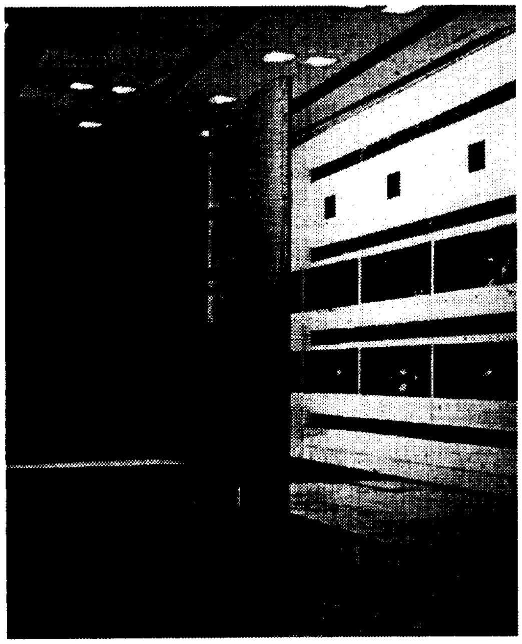

Fig. 11a. Full span flap wing installed in the 14 x 22 Foot Subsonic Tunnel.

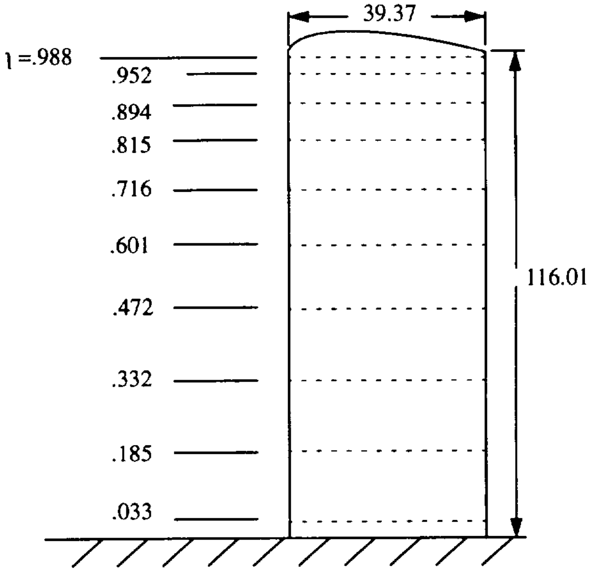

Fig. 11b. 0012 wing pressure tap layout.

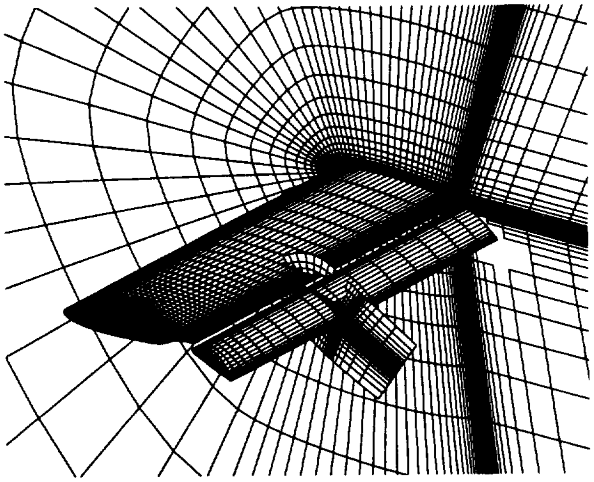

Fig. 12. Partial view of full span flap configuration grids.

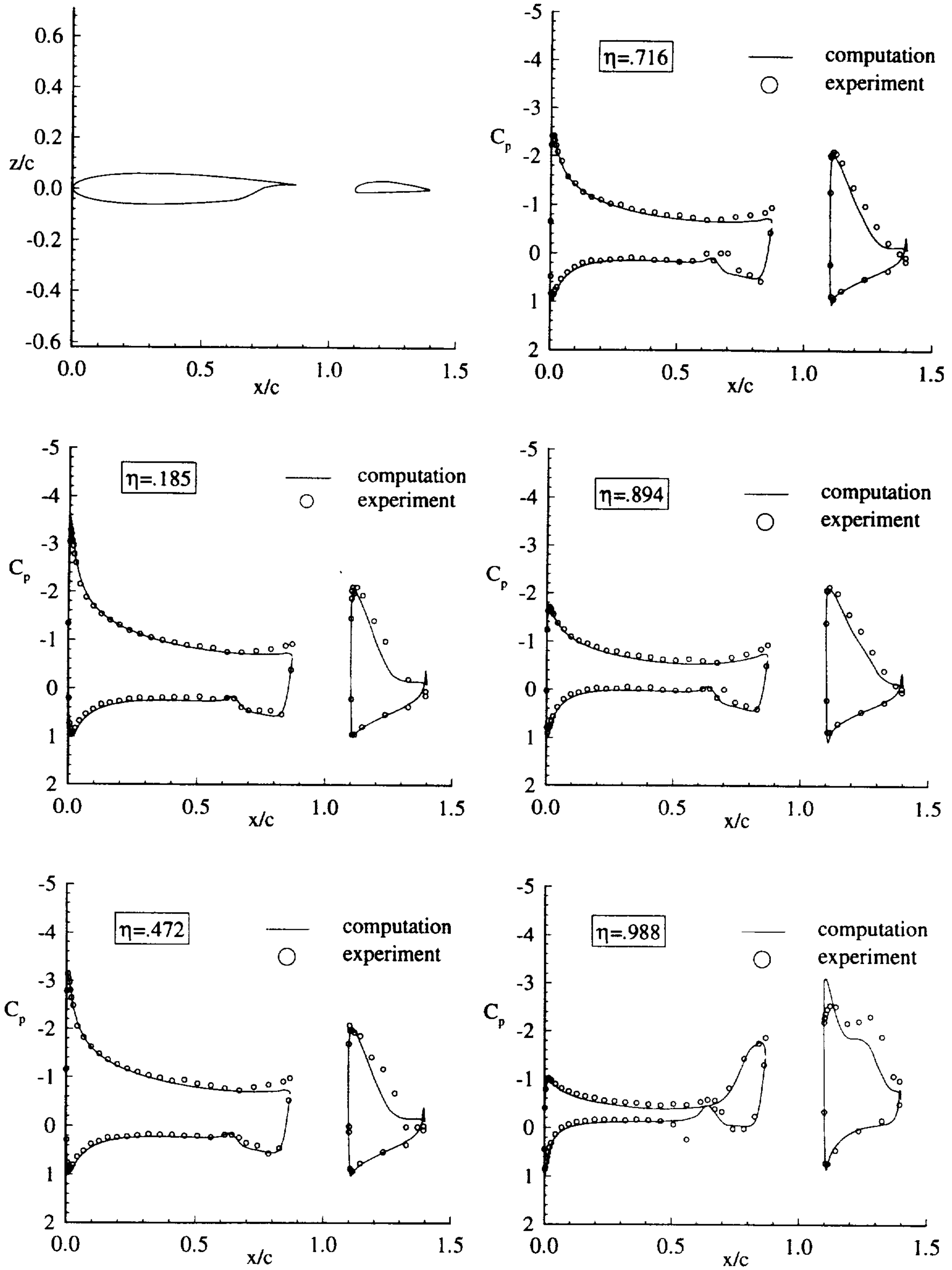

Fig. 13a. Pressure distribution for the full span flap wing, α = 4°.

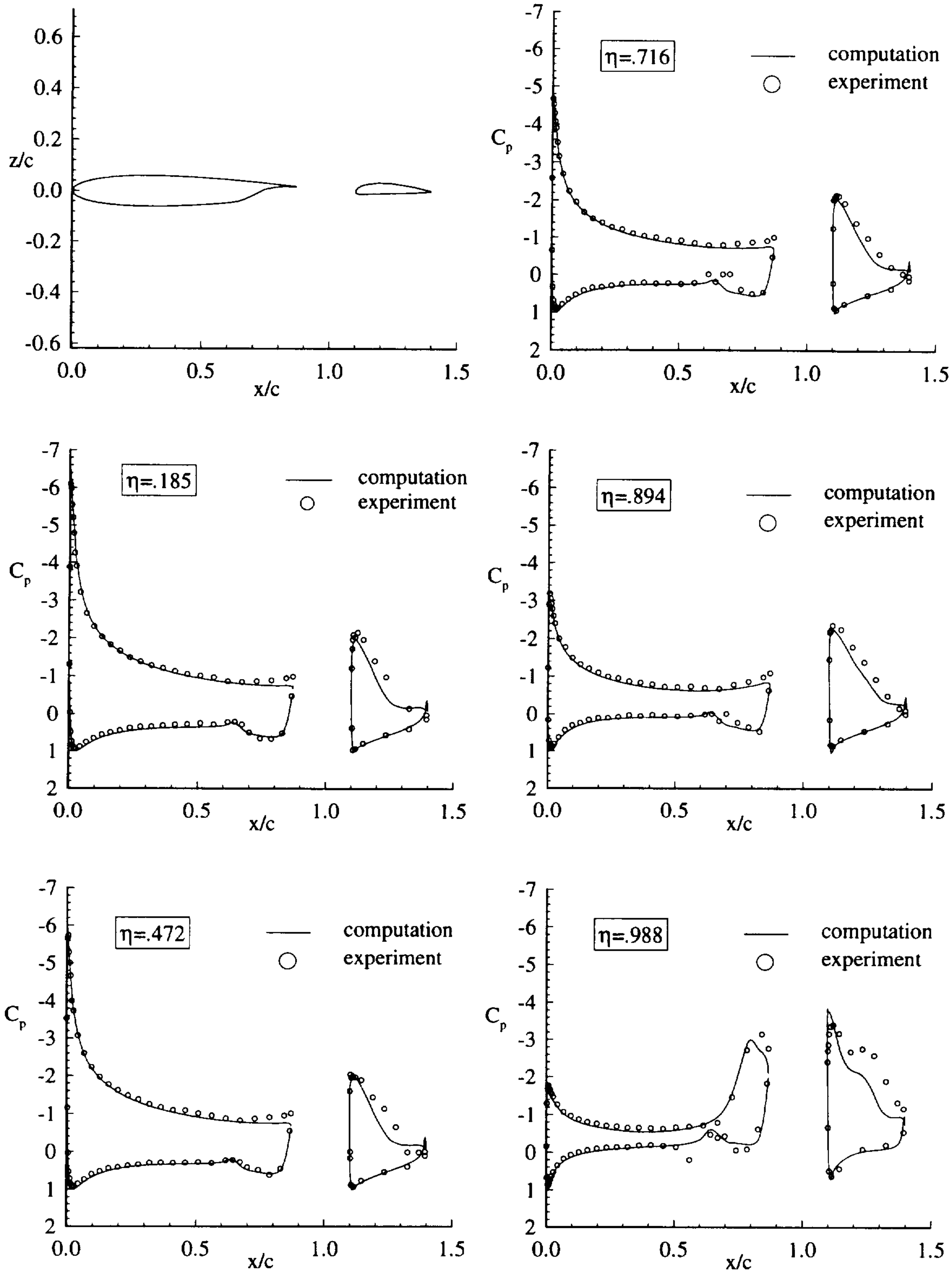

Fig. 13b. Pressure distribution for the full span flap wing, α = 8°.

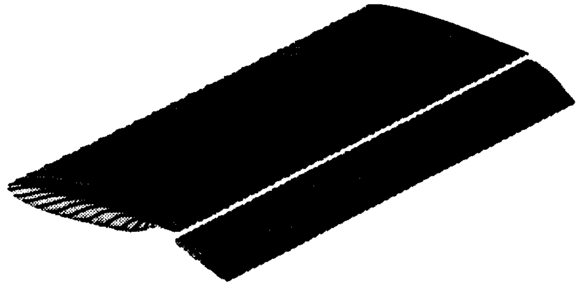

Fig. 14a. Surface streamlines for the full span flap wing, α = 4°.

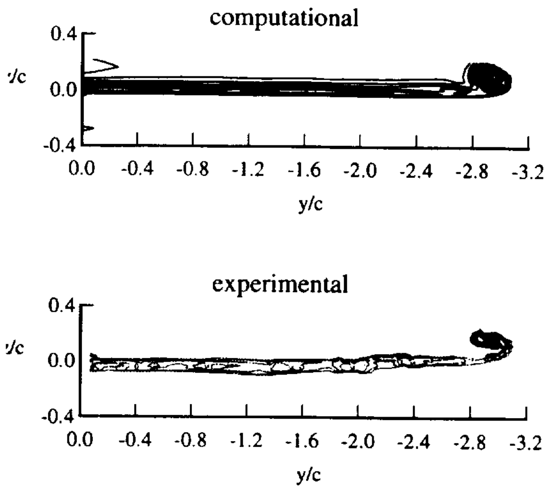

Fig. 15a. Total pressure coefficient contours, α = 4°, 0.1c aft of the flap trailing edge.

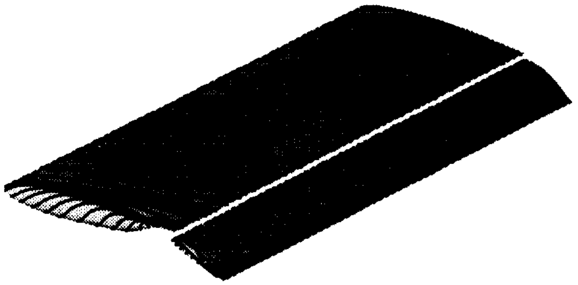

Fig. 14b. Surface streamlines for the full span flap wing, α = 8°.

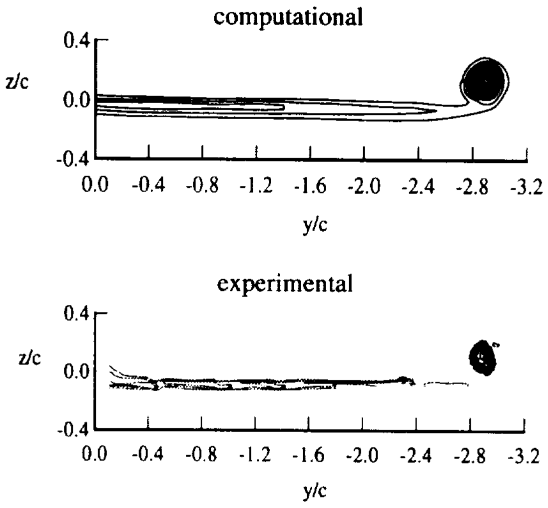

Fig. 15b. Total pressure coefficient contours, α =4°, 0.5c aft of the flap trailing edge.

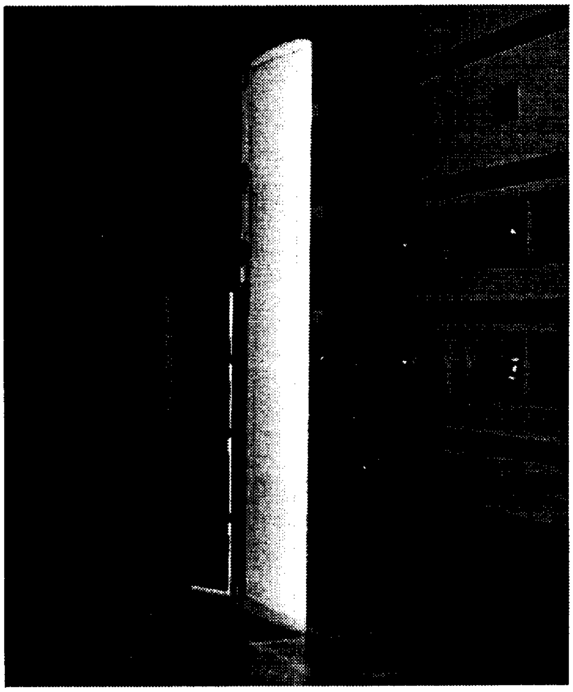

Fig. 16. Partial span flap wing mounted in the 14 x 22 Foot Subsonic Tunnel

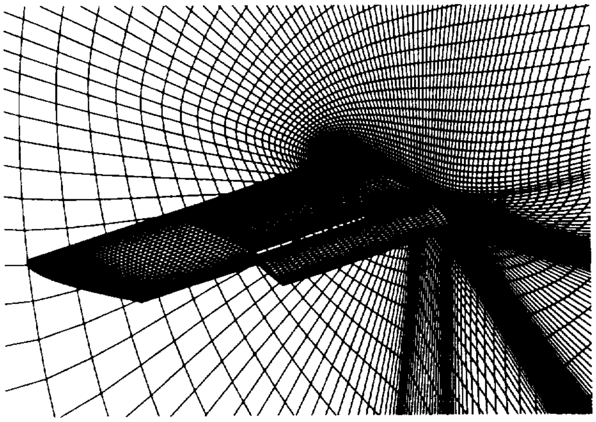

Fig. 17. Partial view of partial span flap configuration grids.

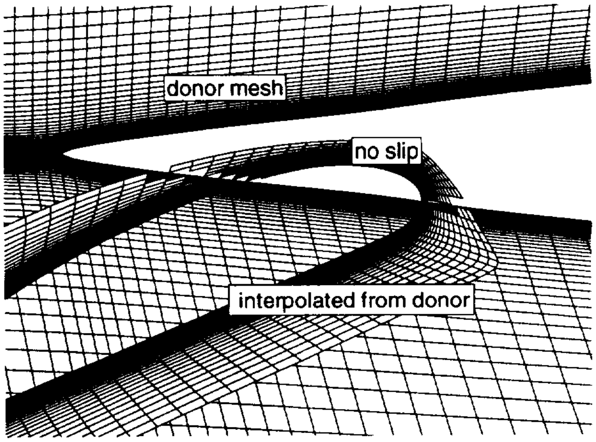

Fig. 18. Partial span flap juncture region interpolation scheme.

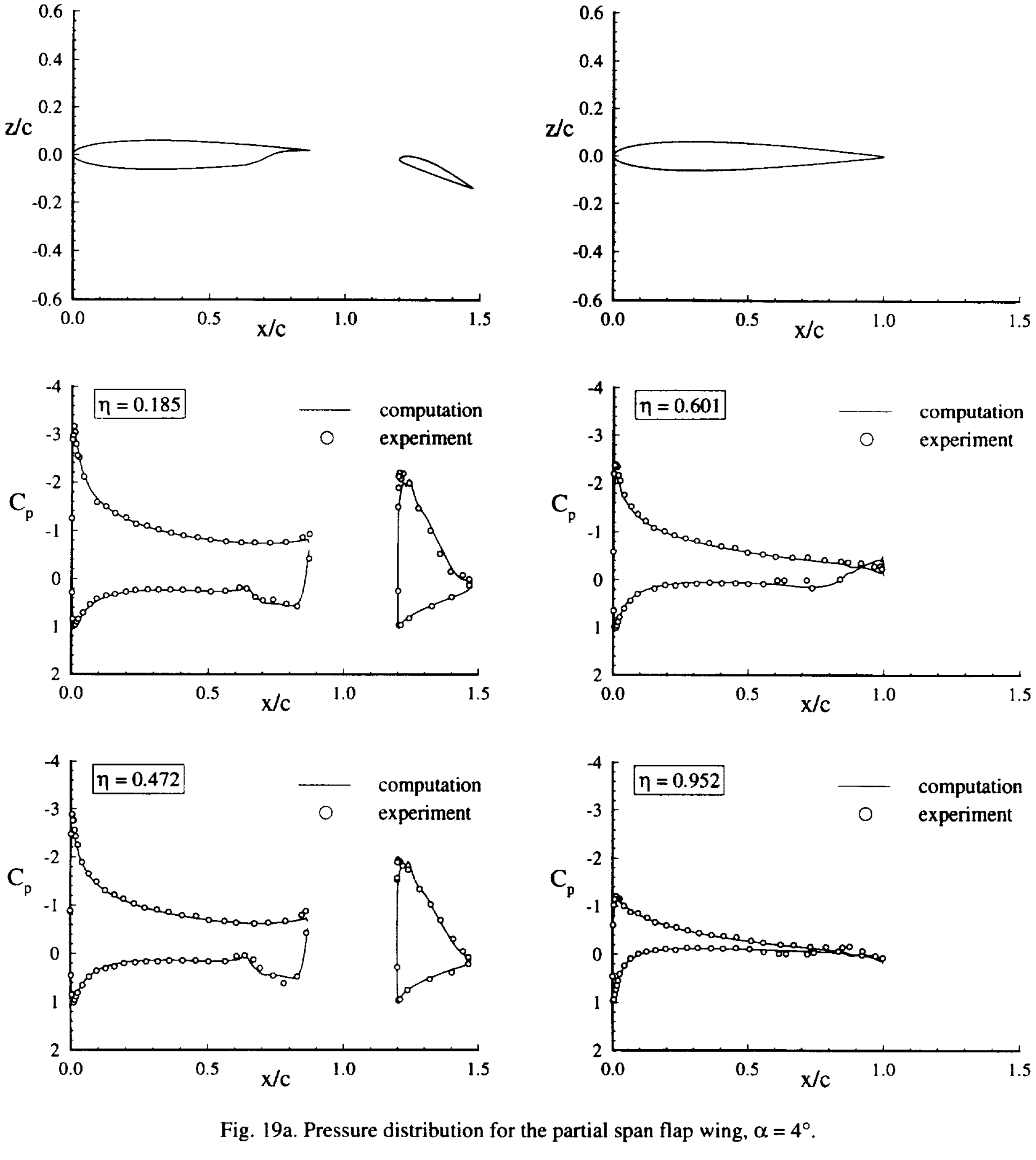

Fig. 19a. Pressure distribution for the partial span flap wing, α = 4°.

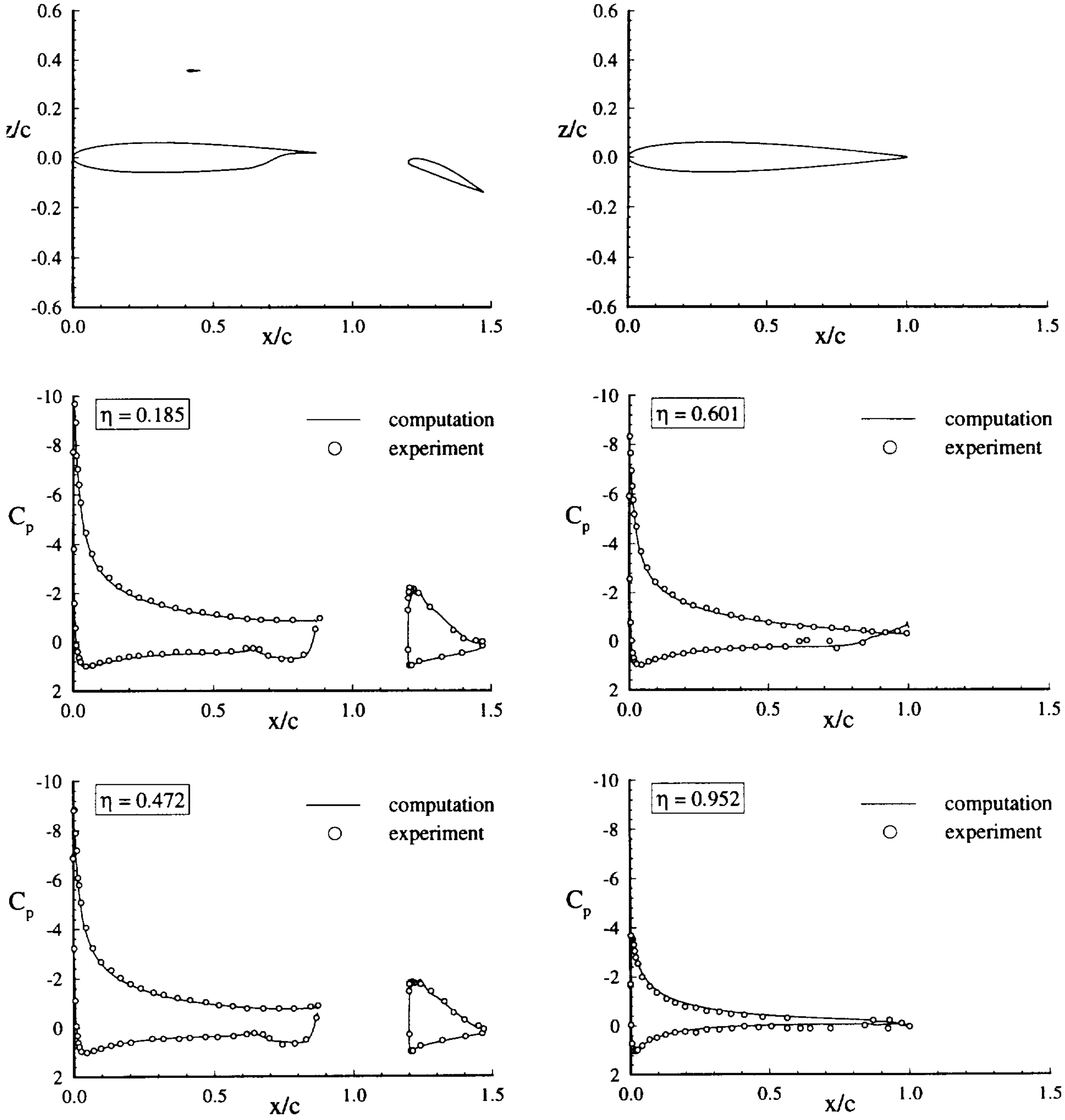

Fig. 19b. Pressure distribution for the partial span flap wing, $\alpha = 12°$.

Fig. 20a. Surface streamlines for the partial span flap wing, α = 4°.

Fig. 20b. Surface streamlines for the partial span flap wing, α = 12°.

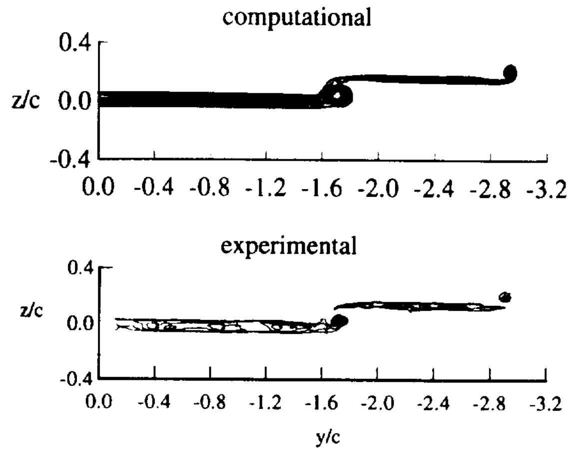

Fig. 21a. Total pressure coefficient contours, α = 4°, 0.1c aft of the flap trailing edge.

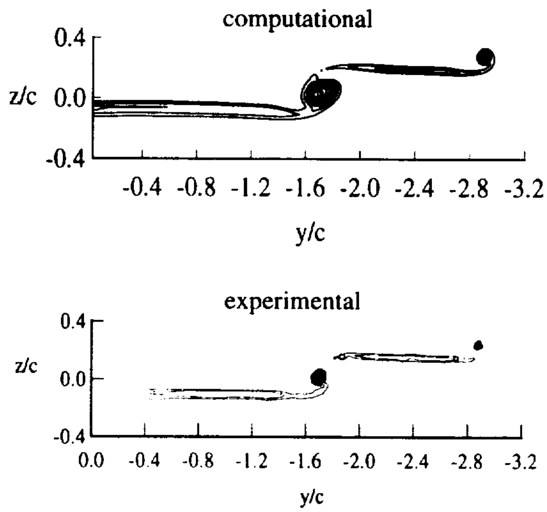

Fig. 21b. Total pressure coefficient contours, α = 4°, 0.5c aft of the flap trailing edge.